TECHNICAL ARTICLE

Characterizing Laser-Modified Microstructures and Electrical and Mechanical Properties of Al-15.3%Si(wt.%) Alloys

Najma Bashir and Azmat Iqbal

Characterization of metallic alloys is of significant interest for fundamental and practical prospects. In this manuscript, we report on the laser-ablation-modified electrical and mechanical properties of Al-15.3%Si(wt.%) alloys correlated with the grain refinement and micro/nanostructuring subjected to various KrF excimer laser pulses. Herein, the irradiation was performed in air at atmospheric pressure by varying laser pulses ranging from 100 to 500. For different laser pulses, the variation in the peak intensities, crystallite sizes, and dislocation line densities were investigated by using XRD techniques. The maximum decrease in grain size (21.21 nm) at 300 laser pulses and maximum increase in grain size (31.6 nm) at 500 laser pulses is observed. Surface morphological changes reveal that irradiated targets are modified by craters, cones, and molten, redeposit material in the form of ripples. Hydrodynamic sputtering, splashing, and exfoliation are the dominant ablation mechanisms. Non-uniform heat conduction takes place on the surfaces in the form of laser-induced cellular or columnar surface structures at maximum pulses. Four-Point Probe revealed that electrical resistivity increases firstly up to 300 laser pulses but at 500 pulses, an abrupt decrease in electrical resistivity is observed. The hardness was tested in three different zones, and it was discovered that the highest hardness was present in all samples of the heat-affected zone. The un-irradiated sample had a hardness value of 91.4 HV, which increased to 127.6 HV when the intensity of laser pulses was raised to 300. Irradiated samples with 400 and 500 laser pulses had lower hardness and dislocation defect density, which was attributed to irradiation-induced annealing. The results are believed to be beneficial in the surface engineering of materials for practical applications such as the electronics, automobile, and aerospace industries. Particularly, they are more important in the automotive body structuring and aviation sector because of their excellent role in providing fuel saving and preventing spare parts from corrosion resistance.

Keywords	AlSi alloys, electrical properties, laser irradiation, microstructures, microhardness

1. Introduction

Laser-assisted modification and characterization is a promising materials processing experimental technique which is extremely beneficial for the investigation and tunability of morphological, structural, and mechanical properties of materials, such as metals, alloys, and ceramics. Lasers can deliver enormous amount of energy to a spatially confined region of material to induce localized changes in surface morphology, crystal structure and chemical properties through material removal by heating or ablation. This is done owing to the elegant feature of lasers by precisely delivering the energy to the materials surface and interior part; thus, making lasers a fascinating experimental tool to explore and modify the properties of materials for the diverse applications. These include pulsed laser deposition (Ref 1), laser-induced breakdown spectroscopy (Ref 2), nanoparticle manufacturing (Ref 3), microelectronics (Ref 4), and micromachining (Ref 5). Significant work by using laser techniques has been done in the morphological manipulation of Al alloys, including surface structuring, annealing, welding, hardening, cladding, alloying, and melting (Ref 6, 7). Laser-assisted tuning of surface microstructures of materials leads to modification of several properties, which cannot be achieved using traditional processing techniques. These changes result from fast rates of heating/cooling and temperature gradients when a high-power laser beam interacts with a target material. There is a possibility of improvement in corrosion resistance (Ref 8), mechanical strength, and tribological properties of irradiated material (Ref 7).

AlSi alloy is an important engineering material that has excellent mechanical properties because of low density, good strength, and high corrosion resistance. These outstanding properties make AlSi and their alloys promising candidates for various industrial applications such as electronics, transportation machinery, automotive, and aviation space (Ref 8). Laser remelting produces a unique surface structure in AlSi-based cast alloys. Because of the huge difference in wear between the hard silicon phase and the malleable aluminum phase,

Najma Bashir, Department of Physics, University of Engineering and Technology Lahore, Lahore, Pakistan; and **Azmat Iqbal**, Department of Physics, Faculty of Engineering and Applied Sciences, Riphah International University Islamabad, Islamabad, Pakistan. Contact e-mail: azmatiqbal786@gmail.com.

microfluidic cellular formations are formed after melting. This topography increases the microhardness of aluminum alloys and is appropriate for engine applications (Ref 9). Susnik (Ref 10) reported that Nd: YAG (Neodymium Yttrium Aluminum Garnet) laser annealing creates a very thin melting layer on the surface of aluminum alloys, which is rapidly re-crystallized to alleviate internal stresses and defects and increases its crystallinity and microhardness. Biswas et al. (Ref 11) explored the impact of laser-assisted surface remelting (LSR) on Al-11%Si alloy. They found that microstructures of irradiated samples turned into a fine-grained structure and improved the wear and corrosion resistance as well as microhardness of about 85 VHN as compared to 55 VHN of the as-received Al-11%Si alloy. Ammar et al. (Ref 12) used a laser surface hardening technique in order to study the microstructure and microhardness (HV) of hypereutectic (Al-18 wt.%Si) alloy by using Nd: YAG) laser. The results disclosed that the laser-irradiated samples had greatly affected eutectic silicon morphology and enhanced the microhardness from 77HV (untreated sample) to 104HV. Zeyad et al. (Ref 13) exploited a pulsed Nd: glass laser to improve the microhardness of Al-25%Si. They studied that the microhardness of Al-25%Si was increased from 105HV up to 242HV through the laser surface melting technique. Mohammed (Ref 14) studied the laser surface modification of aluminum alloys (2024, 390, 7075) by using pulsed Nd: glass laser with energies (1, 1.2, 1.5)mJ and pulse duration (300 μs). The results revealed an increase in laser energy caused to increase in microhardness and wear resistance of the treated alloys. Maryam and Bashir (Ref 15) explored the role of Nd: YAG laser on the modification of structural parameters and hardness of 7178 aluminum alloy. They reported that microstructures of the irradiated alloy were greatly influenced by increasing laser shots in form of ripples and pits. These changes in the microstructures of irradiated samples increased the microhardness of 7178 aluminum alloy. Abbas et al. (Ref 16) studied the microstructures, hardness and wear resistivity of Al-12%Si alloy by using pulsed Nd:YAG laser of different energies, (600, 700, 800, 900 and 1000) mJ. They concluded that fine grain alpha Al microstructures were achieved with increasing laser energies that lead to an increase in wear resistance and hardness of treated samples up to 65%.

The main aim of this experimental work is to investigate the laser-assisted irradiation effects on the hardness of Al-15.3%Si(wt.%) alloy and to find a correlation between their microstructures, morphological, electrical, and mechanical properties using 100 to 500 laser pulses (Table 1).

2. Experiment and Methodology

In our experimental work (Fig. 1), KrF (krypton fluoride) excimer laser (Model EX50 GAM LASER INC, USA) was used to perform ablation experiments with the target samples of AlSi alloys. The laser has a rectangular beam size of 9×4 mm, a pulse energy of 20 mJ, a wavelength of 248 nm, and a pulse duration of 20 ns. The selected sample of AlSi alloy for the research work is a commercially available LM30. The composition (nominal) of the target alloy is given in Table 2. From the "as-received" aluminum alloy sheet of 30 mm thickness and 4 cm radius, six square-shaped samples were sliced mechanically. Proceeding to laser treatments of the selected samples, the first step was grinding and polishing of the samples to a minimum value of roughness of 10 nm. During polishing, the samples were thoroughly cleaned with ethanol and water to remove the contamination on the surface and finally placed in an ultrasonic cleaner for 30 min. These polished samples were mounted in a target holder in front of the laser beam which was focused on the target surface at 90° angle with a Convex lens (f = 20 cm) (from Edmund Optics Inc. in Singapore) as shown in Fig. 1. Laser pulses were fired at targets at a repetition rate of 20 Hz in the air at room temperature, with a spacing of 1 mm between each pulse. For a single laser pulse, the target surface was irradiated with the spot size of 0.02 cm^2. At the spot of focus, the fluence of laser irradiation was 1 J/cm^2 at power density of 5×10^7 W cm^{-2}.

The experiment was performed at constant fluence by using the following formula:

$$\text{Fluence} = \text{Energy}(E)/\text{Spot Area}(A) \quad \text{(Eq 1)}$$

where E is the incident laser beam energy measured in mJ and A is the focused-spot area or the beam-spot size for pulse (single) irradiation measured in cm^2 and was about 0.02 cm^2 in our case. Laser beam power density is found by the following relation,

$$\text{Power density} = \text{Power}/\text{Area or spot size} \quad \text{(Eq 2)}$$

where power = E/t, E = 20 mJ, pulse duration t = 20 ns. Using these values, we find the power of laser beam is 1×10^6 J. With further calculations, we obtained laser beam power density of 5×10^7 W cm^{-2}.

The following equation is used to find out the threshold of laser ablation for the target material (Ref 17).

$$F_{th} = \rho L_v a^{1/2} t_p^{1/2} \quad \text{(Eq 3)}$$

where the heat of vaporization/mass (latent) is denoted by L_v (Ref 18), ρ is the density of a material, t_p is pulse duration, and "a" is the diffusivity coefficient (thermal) of the target material. The following equation can be employed to determine the value of thermal diffusivity (Ref 17).

$$a = K/\rho C \quad \text{(Eq 4)}$$

Here, ρ = 2.51 g cm^{-3} (Ref 19), the thermal conductivity K = 158.2 W/mK) (Ref 20), and the specific heat capacity C is (885.83 J/kg K) (Ref 20) of Al-15.3%Si (wt.%) target alloy. By substituting the stated values in Eq 4, we obtained a value of
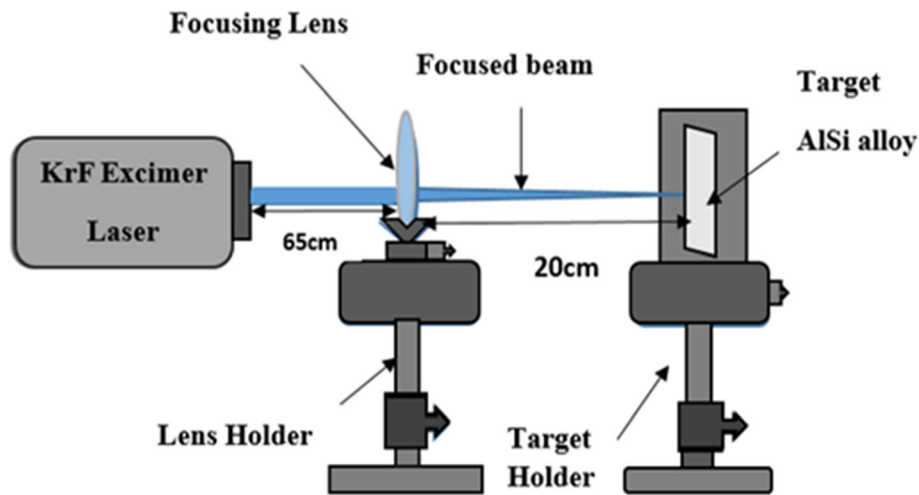
Table 1   Major parameters of KrF excimer laser (Model EX50 GAM LASER INC, USA)

Parameters	Specifications
Laser energy	20 mJ
Laser wavelength	248 nm
Pulse repetition rate	20 pulses per second
Beam size at exit (rectangular)	9×4 mm
Pulse duration or spot size	20 ns
Spot size or area of beam	0.02 cm^2
UV lens focal length	20 cm
Operating temperature	300 K
Fluence	1 J/cm^2
Power density	5×10^7 W cm^{-2}
Number of pulses	100, 200, 300, 400, 500

Fig. 1 The schematic diagram of experimental apparatus of KrF excimer laser

Table 2 Chemical composition of aluminum silicon alloy

Alloy	Al	Si	Fe	Zn	Mg	Mn	Cu	Ti	Sn
Al-15.3%Si (wt%)	79.5	15.3	3.20	0.960	0.548	0.83	0.520	0.049	00.031

diffusivity, $a = 0.31726$ s^{-1} cm^2. Afterward, by using $\rho = 2.51$ g cm^{-3} $a = 0.7115$ s^{-1} cm^2, $Lv = 499.2$ J g^{-1}, and $t_p = 20 \times 10^{-9}$ s in Eq 3, the obtained value of threshold fluence for laser ablation for target material is 1.49 J cm^2.

Afterward, we utilized the laser-ablated AlSi specimens for the investigation of their modified properties utilizing a range of characterization methods. For the investigation of microstructure of the irradiated samples, we utilized LM 6000 (Optical Microscope Leica). To examine the surface structure and morphology of the laser-irradiated Al-15.3%Si (wt.%) alloy alloys, we used a scanning electron microscope (JEOL JSM-6480 LV, JEOL Ltd., Tokyo, Japan). The XRD (D8 Discover, Bruker, Germany) analysis was carried out to find the crystallographic structures, crystalline sizes, dislocation densities, and strains. Meanwhile, electrical resistivity is typically measured with four-point probe techniques (Keithley 2182 Voltage Source). The surface microhardness was evaluated using a Vickers hardness tester (Zwick/Roell ZHU-5030) fitted with a diamond indenter of pyramid shape. The test was performed at room temperature with a 200 g load for 15 s of dentation duration.

3. Results and Discussion

3.1 Structural Analysis

Figure 2(a) illustrates the XRD patterns of an un-irradiated and irradiated Al- 15.3%Si(wt.%) alloy for 100 to 500 laser pulses. Figure 2(b) depicts a magnified view of Al (200) peak, which demonstrates the difference in peak intensity and peak position between untreated and treated targets.

The XRD spectrum of untreated Al-15.3%Si (wt.%) alloy reveals the diffraction peaks of Al at 38.493, 44.527, 65.584, 77.525. These correspond, respectively, to the (111), (200),

(220), and (311) planes of face-centered cubic aluminum (Pattern No. 01-089-4037). The diffraction peaks of Si at 28.316, 56.416, 47.520 correspond to the (111), (220), (310) planes ((Pattern No. 01–089-4037). After the XRD examination of samples, the following informative features are prominent in Fig. 2(a) and (b). (i) Some Bragg reflections are clearly visible from the Al and Si crystalline phases. (ii) Bragg reflections of Mg, Fe, Zn, Mn, Cu, Ti and Sn are not visible because of their very minute concentrations, or their Bragg reflections might be overlapped with that of the Al phase. Figure 2 shows that the peak intensity of Aluminum with (200) plane orientation is more prominent intensity as compared to Al(111) plane. Similar domination of peak intensity Al(200) is noticed by Kalsoom et al. (Ref 21). Bow et al. (Ref 22) reported that increasing silicon content in Al alloy leads to an increase in the ratio of peak intensities of the plane (200) to (111). This indicates a monotonous increase in the number of Al(200) structure as compared to that of the Al (111) structure. Furthermore, there is no sharp change seen in peak intensities of (220) and (310) planes of Si with changing laser pulses. Figure 2(a) also exhibits that by increasing laser pulses from 100 to 300, there is a decrease in the peak intensity of plane (200) of irradiated Al-15.3%Si(wt.%) alloy seen as compared to the peak intensity of plane (200) of un-irradiated Al-15.3%Si(wt.%) alloy. The reason might be the thermal agitation induced in the aluminum alloy via UV radiation. Basically, crystal planes are composed of identical repetitive items according to the superposition of bases on periodical Bravais lattice. Due to these repetitions, the smooth and flat XRD reflected intensities are seen at certain temperatures. If the temperature of the material enhances due to heating, then vibrational amplitude of the atoms increases and atoms show a little deviation from their original places. Consequently, more extensive roughen of diffraction planes come into view and is a cause of lowering in the XRD reflected intensities (Ref 23). The distortions of the atomic planes (lattice
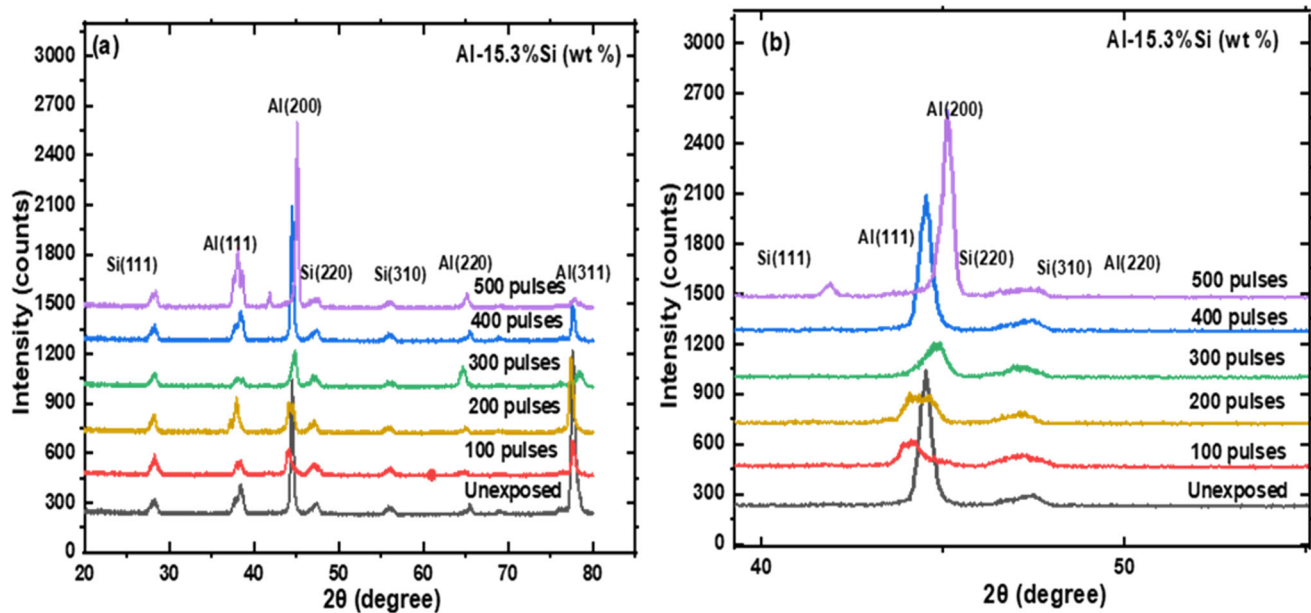
Fig. 2 (a-b) XRD data of unexposed and exposed Al-15.3%Si (wt.%) alloy for 100 to 500 laser pulses, (b) a magnified view of Al(200) peak

strains) produced by the residual stresses are also one of the main reasons to create change in the d-spacing of the diffraction planes, resulting in peak shifting or reduction in the intensity of planes (Ref 24). Further, increasing laser pulses from 400 to 500, an increase in peak intensity of (200) is observed. This is understandable as at 500 laser pulses, crystalline defects are reduced. Laser irradiation on the surface of Al-15.3%Si (wt.%) alloy generates two types of residual stresses, i.e., tensile and compressive residual stresses. These stresses are significations of peak shifting in XRD patterns. Peak shifting toward the higher values (right side) of Bragg's angles is a sign of tensile strain or lattice relaxation (Ref 25), whereas shifting toward lower Bragg's angles (left side) is an indication of compressive stresses or lattice strain (Fig. 2b).

Using Scherrer formula, the crystalline size was determined from the peak broadening patterns of the diffraction planes (Ref 26).

$$\text{Crystallite size (D)} = K\lambda/(\beta \cos\theta) \qquad \text{(Eq 5)}$$

where constant (K) is called shape factor, approximately equal to 0.94, θ (in radians) indicates Bragg's angle, λ is the incident X-rays wavelength, and β (in radians) indicates Full Width at Half Maximum (FWHM) of diffracted X-rays intensity peaks. The dislocation line density (δ) can be calculated by Williamson and Smallman's equation (Ref 27).

$$\delta = 1/(D)^2 \qquad \text{(Eq 6)}$$

The strain ε (average) induced by laser irradiation in the target material due to crystal imperfection and distortion can be calculated by using the Wilson Stokes equation (Ref 28).

$$\varepsilon = \beta/4\tan\theta \qquad \text{(Eq 7)}$$

The occurrence of residual stresses for Al-15.3%Si (wt.%) alloy is calculated by taking the product of Young's modulus (E) with residual strain (ε) of the corresponding phase. The laser-induced stresses σ are calculated as (Ref 29).

$$\sigma = \varepsilon E \qquad \text{(Eq 8)}$$

where Young modulus is denoted by E, which is equal to 70 GPa for Al (Ref 21) and 74 GPa for Al 15.3%Si (wt.%) alloy (Ref 30).

Figure 3(a) depicts the variation in average crystallite size of Al 15.3%Si(wt.%) alloy after ablation in air for 100 to 500 laser pulses. The average value of crystallite size of un-irradiated samples is 29.44 nm. The minimum observed crystallite size for irradiated samples is 21.21 nm at 300 laser pulses, which is smaller than un-irradiated samples. Maximum average crystallite size of irradiated samples (31.6 nm) is found at 500 laser pulses. It is clear from Fig. 3(a) that crystallite size reduces with the increasing laser pulses up to 300 and an abrupt increase in crystallite size is found at 400 to 500 laser pulses. During laser–matter interaction, long-range internal stresses are induced in the interstitial position of the crystal and caused the lattice distortion (strain). This lattice distortion generates residual stresses in the material that can further produce lattice defects such as vacancies, stacking faults, planar faults, or twin boundaries and cause reduction in crystallite size (Ref 31). A major increase in crystallite size is noted during the 500 laser pulses. These higher numbers of pulses cause the melting of samples, and on cooling, the re-solidification occurs. This re-solidification is attributed to the annealing of samples in which rearrangement, reduction, or annihilation of dislocations occurs through re-crystallization processes and leads to increment in grain size (Ref 32).

Figure 3(b) shows a graph between the dislocation line densities and laser pulses for Al-15.3%Si (wt.%). The average value of dislocation line densities of un-irradiated samples is 11.55×10^{14} lines/m^2. The dislocation density appears to increase at 100 to 300 laser pulses for irradiated alloy and beyond 300 pulses it depicts a progressive decline. The maximum increment in average dislocation line density of irradiated samples is 22.22×10^{14} lines/m^2 found at 300 laser pulses which is greater than un-irradiated samples (11.55×10^{14} lines/m^2) and then starts the decreasing trend till it attains a minimum value of 10.01×10^{14} (lines/m^2) for 500 laser pulses. It is reasonable by taking into consideration
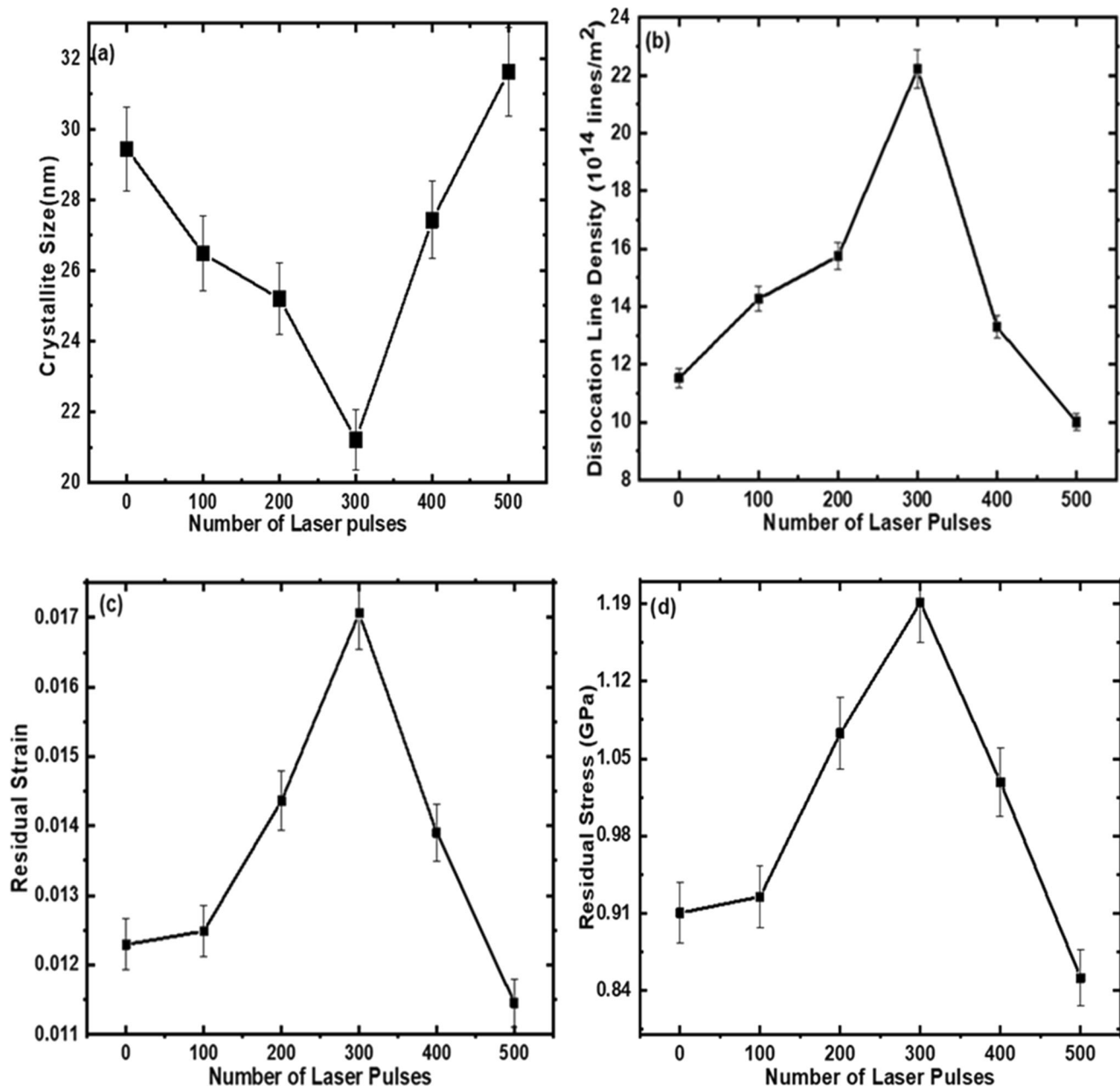
Fig. 3 (a-d) XRD patterns of Al-15.3%Si (wt %) surface for 100 to 500 laser pulses (a) crystallite size variation, (b) dislocation density variation, (c) strain variation, (d) Residual stress variation

that more heat energy is absorbed by atoms up to 300 pulses. This in turn progressively results in more dislocation lines. However, an increase in the laser pulses intensity/number up to 500, causes the enhancement in temperature. Here, new dislocation lines arise due to laser-matter interaction, while reduction in dislocation lines arise due to recovery via annealing of the samples, which appear to operate at the same time. A dynamic equilibrium between the two processes is established. It is observed that the simultaneous contributions from the two processes cancel the effect of each other for the sample irradiated with 500 laser pulses. Resultantly, the dislocation line density in the irradiated samples of AlSi allows could achieve the status of the pristine un-irradiated sample (Ref 33).

During irradiation, the formation of thermal shocks on the target's surface plays a significant role in crystal development. Lattice defects caused by implanted ions and thermal shocks induced in materials by laser irradiation can lead to variations in residual stress. Thermally excited shocks caused by impinging laser pulse cutoff often result in residual stresses of tensile nature, whereas ion implantation produces residual stresses of compressive nature (Ref 34, 35). The compressive stress seen at l00 to 300 laser pulses is a result of the tiny crystallite size, which slows the slip motion, hence enhancing the material's strength. During irradiation process, a sufficient amount of energy is delivered to the surface of the target material. This raises the surface temperature of the target material, thus causing lattice deformation and a reduction in crystallite size, which in turn generates compressive residual stresses on the

irradiated target (Ref 36-38). Jelani et al. (Ref 39) reported the creation of irradiation pressure in the gigapascals (GPa) range for zirconium subjected to KrF Excimer laser irradiation. This in turn generated compressive residual stresses. Figure 3(c) and (d) depicts the relationship between microstrain and residual stress as a function of intensity of laser pulse variation. As the number of pulses increases from 100 to 300, the residual compressive stress relaxes, with further increase in the number of pulses up to 500, this compressive residual stress is converted into a tensile one.

The relaxation of compressive residual stress and its transformation into tensile residual stress is attributable to crystalline size enhancement caused by laser-induced thermal shock as the number of laser pulses increases. The peak is shifted toward a higher angular position, which confirms the contraction and improvement in the properties of the crystal due to changes in lattice parameters (Ref 25). On the other hand, the shifting of peak toward a lower angular position confirms the expansion of crystal size which suppresses the properties of the crystal due to changes in lattice parameters (Fig. 2b). Results in Fig. 3(a), (b), (c), and (d) show the strong correlation between these and the surface features (SEM micrographs Fig. 5a–j). The establishment and increase in crystal size as well as density of cellular/columnar structures with increasing laser pulses is marked by the relaxation and/or transformation of compressive stresses into tensile ones.

3.2 Surface Morphology

The optical micrographs of an array of laser-irradiated Al-15.3%Si (wt.%) with various laser pulses (100,200,300,400,500) are depicted in Fig. 4(a), (b), (c), (d) and (e). The results show that surface ablation is prominent with the formation of elliptical shape crater. The formation of the crater can be certified as thermally induced ablation arising from the laser-assisted heating, melting, and extensive boiling of the irradiated surface (Ref 40). It has been noticed that if the surface temperature of the target material is greater than the melting point then fusion and evaporation occur. If irradiation energy is greater than the ablation threshold, then ionization occurs which leads to plasma formation. When plasma pressure goes above the surrounding pressure, then melted material is explosively expelled from the surface of the target under the influence of forceful recoil pressure. This leads to the formation of crater (Ref 40). The morphology around the crater is observed in three zones: (1) Laser-irradiated zone, (2) Coarse zone, and (3) Heat-affected zone as shown in Fig. 4(a), (b), (c), (d) and (e). These are described as follows.

(1) Fine zone/laser-irradiated zone: Most of the melt pool is located in this zone (Fig. 5(a), (b), (c), (d) and (e), Flow of melted material is observed at 100 to 300 pulses while the interior of the laser paths paves the way for the growth of cellular structures at 400 and 500 pulses (Fig. 5(i) and (j). This is because of metallic and non-metallic Al-Si systems, in which a non-faceted interface of the alpha Al phase expands faster than the faceted interface of the Si phase under conditions of high cooling rate (Ref 41). Within the melting pool, cellular/columnar structures are observed growing toward the pool's center. The approximate 60 to 100 nm width of Al cellular structure is observed in Fig. 5(i) and (j). Similarly gradual refinement of microstructure is ob-

served from the boundary to the central part of the fine zones.

(2) Coarse zones: These are located at the edge of the melt pool. The average width of about 10 μm for the coarse zones is reported. Compared to fine zones, the length of α -Al is considerably shorter in coarse zone. On the other hand, the width is about twice as great as in fine zones.

(3) Heat-affected zones (HAZs): The HAZ zone is the non-melted area of metal and is about 10–20 nm in diameter and is noticed immediately behind the coarse zones. In the HAZs regions, there is no apparent growth pattern preferring the laser-track axis. In HAZs, the fibrous like Si network was broken into particles, but it is still possible to identify the original network. Moreover, some of the coarse Si particles can also be observed in HAZs zones (Fig. 5a–j).

A detailed examination of irradiation samples indicated that three zones could be distinguished across the melt pool based on the appearance and size of the nano/microstructures. The melt pool track border was examined on both transverse and longitudinal cross sections as shown in SEM micrographs (Fig. 5a–j). For 100 laser pulses (Fig. 5a), discontinuous tracks were seen. These certain discontinuous tracks are due to mainly two reasons, one is non-uniform heat transformation to the target material, and another is partially remelted deposited layers, resulting in variations in the depth and shape of the melt pool (Ref 42). Figure 5(b) indicates the re-deposition in the boundary area. It shows that the material is ablated in bulk. The non-uniform deposition of the ablated material is caused by disturbing the sharpness of the boundary of the ablation zone. Thermal stresses (shockwave) drive the material on the surface due to instant heat conduction, and then the material is re-solidified at the surface. There is a non-symmetrical and non-uniform ejection of material, so asperities, turbulent features, and craters are developed on the target surface (Ref 43). By increasing laser pulses from 100 to 200, the UV radiations generate more defects in the crater region and are responsible for more absorption and expulsion of material in the irradiated areas. Then busted bubbles and perforations are appearing on the surface of the material as shown in Fig. 5(c) and (d). These busted bubbles are signs of strong evaporation. The central portion of Fig. 5(e) and (f) indicates some sort of splashing of the material due to the increasing number of laser pulses up to 300. The flow in a random direction exhibits the non-uniformity in heat conduction. The localized laser heating originates large temperature gradients that are followed by rapid self-quenching, and produces highly non-equilibrium structures. These temperature gradients produce thermal stresses and acoustic waves. The material tries to maintain some periodicity during flow, but non-uniform thermal stresses and heating produce randomness in the flow (Ref 44). Maximum heating provides maximum molten flow, thus causing hydrodynamic sputtering. Micron size droplet, perforation, re-solidification, craters and bursting bubbles appear as surface modifications as shown in Fig. 5(f). At 400 laser pulses, the surface morphology comes out as an entirely different picture other than those obtained at 100 to 300 irradiances. The primary Al phase and nanoscale hypereutectic Al-Si network were observed and formed a fine substructure. This new structure is composed of Al and is covered with white fibrous Si particles and gives phase transformation into cellular/colum-
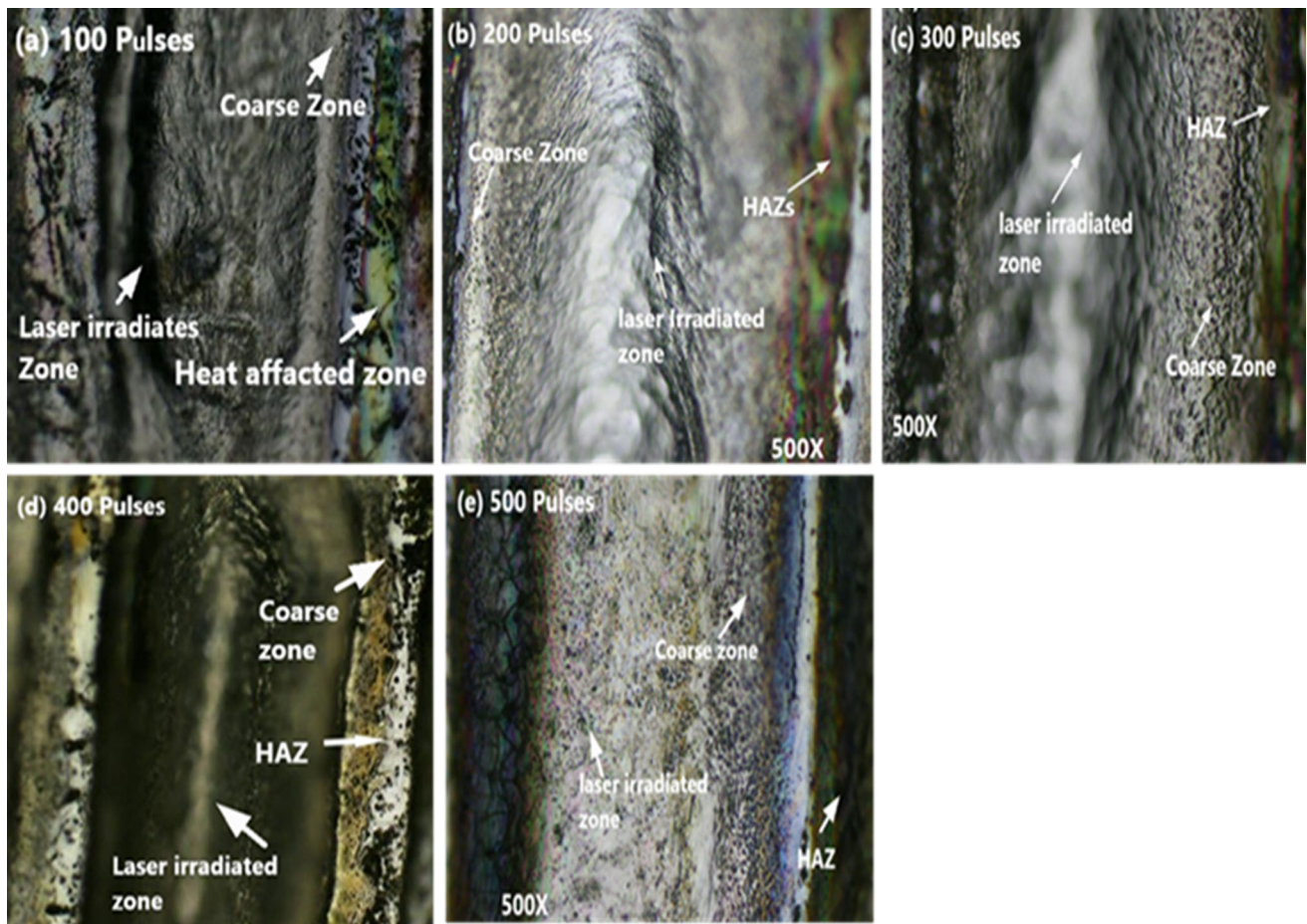
Fig. 4 (a-e) Optical micrographs of laser-irradiated Al-15.3%Si (wt %) alloy exposed to 100—500 pulses. (a) 100 pulses; (b) 200 pulses; (c) 300 pulses; (d) 400 pulses; (e) 500 pulses

nar structures (Fig. 5g and h). This cellular structure proposes a well-built irradiation region in the center, and a modest irradiation region at the periphery. In such cases, the center might be extremely heated and perhaps a sign of explosive boiling. Figure 5(h) shows that there is an irregular melting pattern at the edges of the crater. Furthermore, the irradiated area of the sample has many small blow holes, which are due to escaping of atmospheric gas that originated from a violent ablation process. White droplets can also be seen in Fig. 5(h) which is a sign of hydrodynamic sputtering.

The most informative and important features of irradiated samples are shown in Fig. 5(i) and (j). By increasing the number of laser pulses up to 500, the center of the sample would be heated-up at an extreme rate and resulting an increase in the temperature of the absorbing region so fast that it may exceed the melting point of the sample and quickly convert the irradiated part of samples into the liquid state. When laser pulses cease after exposure, transportation or interaction of electrons with lattices also ceases, then a quick decrease in the temperature of the sample is seen. This quick increase and decrease in temperature cause epistaxis and re-crystallization of the sample. When very strong laser pulses are fallen on the surface of samples, formation of the plasma becomes compulsory (Ref 45). This plasma becomes one of the reasons for the melting of surface layers and the occurrence of re-crystallization. During this process, grain refinement occurs, and the structure becomes more homogenized. The modifications of the

surface appear in the form of melting and merging of grain boundaries. These crystallization cells are created by an aluminum-based solid solution, with silicon particles located on the cell borders (Ref 46). The sizes of crystallization cells forming the structures of lamellar/cellular hypereutectic (Fig. 5i and j) range between 60 and 100 nm. Analyzing the results presented in Fig. 5(i) and (j), it is likely to conclude that the high velocity thermal excitations induced by the pulsed electron beam leads to the formation of a cellular structure of high velocity crystallization. Mann et al. (Ref 16) reported that laser exposed Al-12%Si alloy displays an elongated cellular or luminar morphology is the result of fast melting and quick solidification. A very quick heat extraction occurs during solidification due to the close contact between the melt and the solid substrate, resulting in extremely fast cooling rates on the order of 105 to 108 k/s. This rapid cooling of the surface layer caused the development of more refined cellular structures from the bulk metal and also improved the surface characteristics. Similar unique microstructures of AlSi10Mg alloy are seen which is the result of the high cooling rate (10 K/s) and thermal gradients that take place in process of SLM (Ref 41). A fine pseudo-eutectic columnar microstructure was also found in laser-cladded hypereutectic Ti-20%Si alloy by Zhang et al. (Ref 47). They concluded that this was due to the rapid cooling rate of the target after laser irradiation. Furthermore, Dinda et al. (Ref 48) also reported that during the fast solidification of a eutectic or hypoeutectic Al-Si alloy, the amount of alpha Al
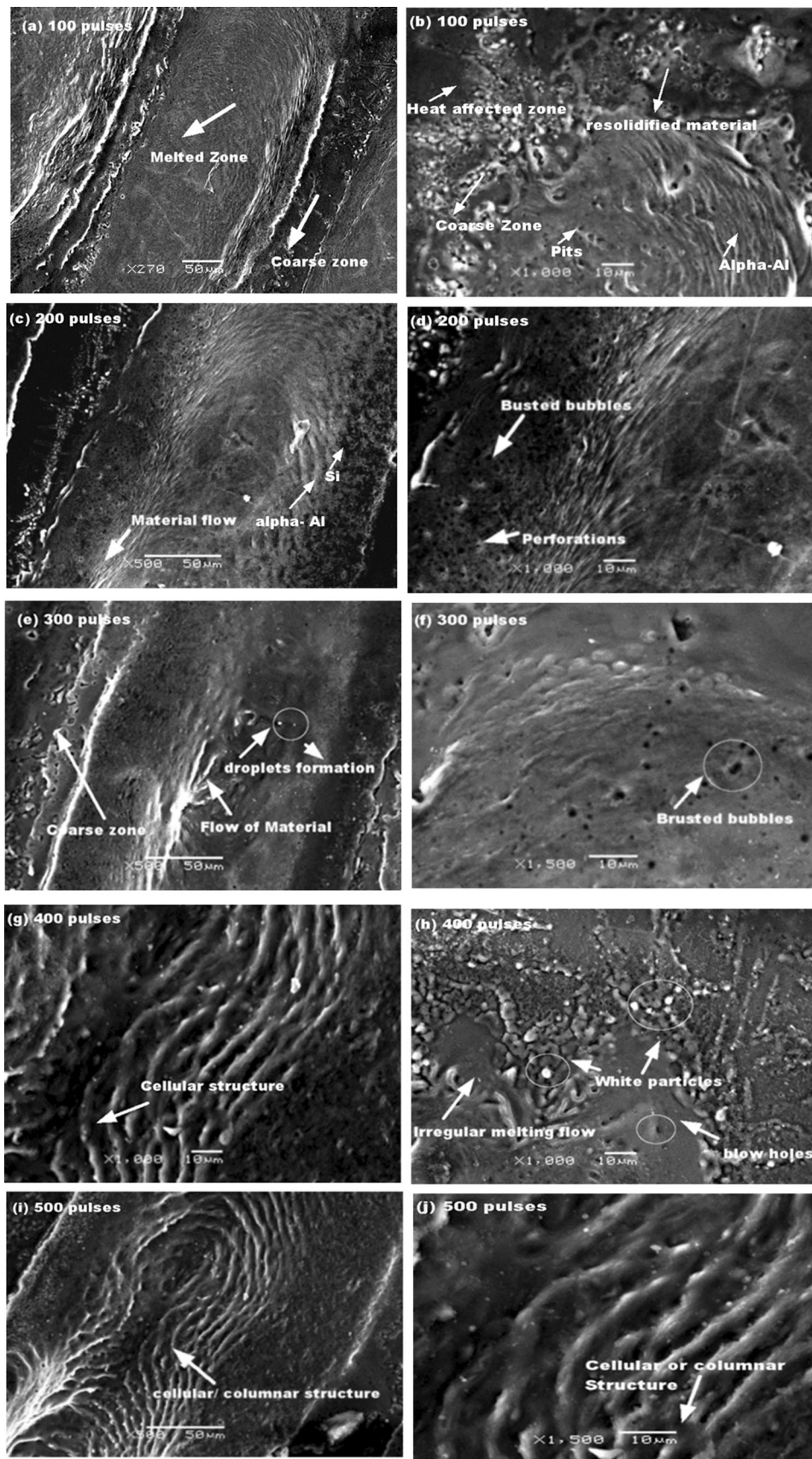
Fig. 5 (a-j) SEM micrographs of laser-irradiated Al-15.3%Si (wt. %) alloy exposed to 100–500 pulses: (a,b) 100 pulses; (c,d) 200 pulses; (e,f) 300 laser pulses;(g,h) 400 pulses;(i,j) 500 pulses, center portion of crater at 500X and edges of crater at 1000X

increases with increasing solidification velocity and results in a fined columnar structures.

3.3 Electrical Resistivity

Four-point probe method is used to determine the changes in an electrical resistivity of the UV irradiated sample of Al-15.3%Si(wt.%) alloy. Electrical resistivity of irradiated alloys is calculated using the given expression (Ref 49).

$$\text{Electrical Resistivity} = F_p \times t \times (V/I) \qquad \text{(Eq 9)}$$

where F_p is correction factor = 1.54563, I is the current between two external probes, V is applied voltage, and t is the specimen thickness. Al-15.3%Si(wt.%) alloy samples were exposed at different values of laser pulses 100, 200, 300, 400, and 500. One of the unexposed samples (0 numbers of pulses) is used as a reference sample.

It is clear from Fig. 6(a) that the electrical resistivity appears to increase at 100 to 300 laser pulses and beyond 300 pulses it depicts a progressive decline. The maximum increment in electrical resistivity of irradiated samples is found at 300 laser pulses which is greater than un-irradiated samples. Then we notice a decrease till it attains a minimum magnitude for 500 laser pulses. Figure 6(b) indicates an exponential decay curve between crystallite size and electrical resistivity with mathematical formulation as given below:

$$\rho = \rho_0 + A_1 * \exp(-(x - x_0)/t_1) \qquad \text{(Eq 10)}$$

With a correlation factor $(R) = 0.999$ and constants, $\rho_0 = 13.37$, $x_0 = 21.21$, $A_1 = 17.14$, $t_1 = 2.42$. The variable x represents crystallite size, and the dependent variable ρ indicates the electrical resistivity. Figure 6(b) shows the maximum increase in electrical resistivity (i.e., 30.52×10^{-7} (Ω–m) at 300 laser pulses for a minimum value of crystallite size (21.21 nm). At 500 laser pulses, the largest drop in electrical resistivity (13.61×10^{-7} (Ω–m)) is found at the maximum value of crystallite size (31.6 nm). Therefore, it is concluded, an increase in electrical resistivity can relate to crystallite size, the smaller the crystallite size, the higher the frequency of scattering defects for the electrons traveling through the lattice. This causes the higher resistance in the flow

of electrons through the lattice (Ref 52). Vopsaroiu et al. (Ref 53) observed a notable exponential relation between grain size and electrical resistivity of CoFe thin films. They observed that films with smaller grain size exhibit high resistivity whereas for the larger-grained specimens, the resistivity drops to the bulk value. These effects are explained using scattering at grain boundaries as well as the bulk scattering center. Moving an electric carrier through a sample containing small grain causes extra scattering at the grain boundaries, resulting in a reduced mean path and an increase in the electrical resistivity. Oleg et al. (Ref 54) showed that grain size effects the electrical resistivity of bulk nanograined Bi_2Te_3 material. They found that electrical resistivity increases with decrease in mean grain size. Moreover, laser-induced damages on the material surface generate thermal stresses and crystal defects and dislocations like lattice vacancies, interstitial and point defects, grain boundaries, stacking faults, as well as voids and craters. This causes decrease in grain size and the increase in electric resistivity (Ref 50, 51). At 500 laser pulses, there is decrease in electrical resistivity observed due to the occurring of pulsed laser annealing that reduces the defect density by the melting, recovery, and re-crystallization mechanism. At a sufficiently high temperature, re-crystallization occurs which produces new strain-free and equiaxed grains with smaller dislocation densities. It could be seen from SEM micrographs (Fig. 5i and j) that at 500 pulses, an entirely new columnar microstructure arises. It is usually accompanied by a decline in resistivity or an enhancement in conductivity of the treated samples (Ref 55). Kaya et al. recently reported similar results for Al-5.7 wt.% Ni eutectic alloy (Ref 56) and Al-7 wt.% Ni hypoeutectic alloy (Ref 57). They reported that electrical resistivity/conductivity highly depended on the microstructure parameters, such as primary and secondary average eutectic spacing. According to their report, the increase in average eutectic spacing values causes a monotonically decline in electrical resistivity and microhardness (Ref 57).

3.4 Microhardness

Vickers hardness testing machine with applied load of 200 g was used to analyze the hardness of Al 15.3%Si(wt.%) alloy
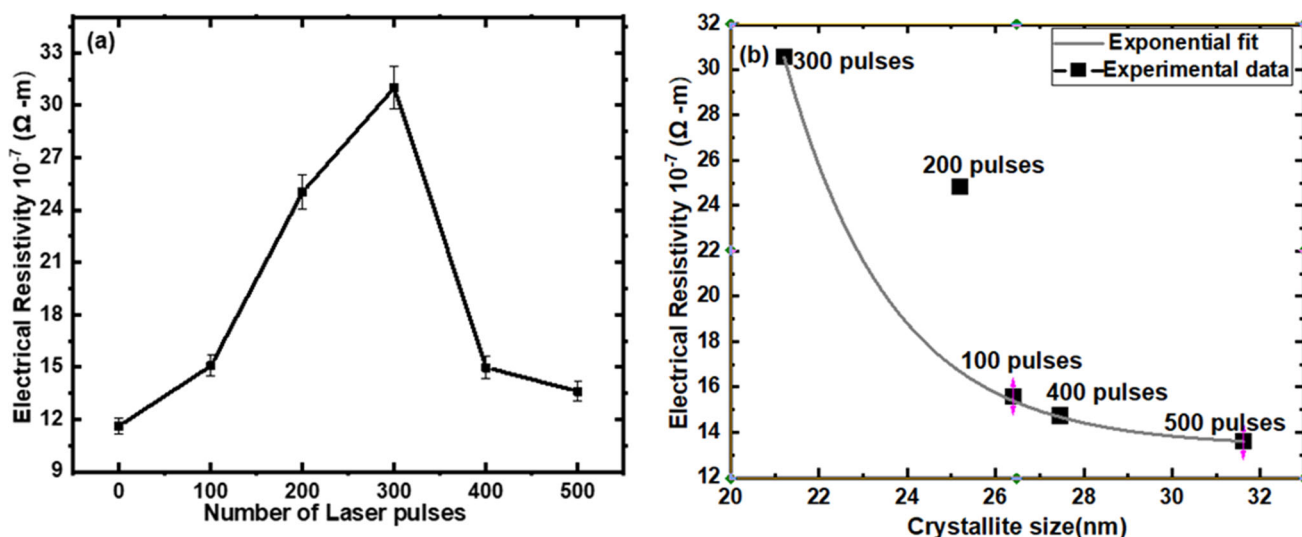
Fig. 6 (a-b) Electrical resistivity of Al-15.3%Si (wt. %) alloy as a function of laser pulses (b) crystallite size

after irradiation with KrF excimer laser in air for 100 to 500 laser pulses (Table 3).

The basic principle to examine material hardness is mainly based on measurement of the resistance of a material to plastic deformations. The average microhardness was taken from the five different points on the irradiated material. It is observed that the surface microhardness was different everywhere on the scope of the same laser-irradiated elliptical spot. So the microhardness profile can be divided into three zones, laser-irradiated zone, heat-affected and base zone. It is observed that hardness in the laser-irradiated zone and the heat-affected zone is affected a lot in comparison with the hardness values of the base zone.

Figure 7(a) shows that for 100 laser pulses, the measured surface hardness of HAZ is 108.8 HV, which is 18.9% higher than the untreated sample. For 200 laser pulses, the surface hardness increases up to 115.4 HV which is 26.1% higher than the un-irradiated alloy. The surface hardness of the target sample irradiated with 300 pulses is found to be 127.6 HV, which is 39.4% more than the un-irradiated samples. The abrupt decline in surface hardness of the sample up to 85.9 HV is observed for 500 pulses. This is 2% less than the hardness of the un-irradiated sample. From the above experimental data (Table 4), it can be seen that the values of hardness in the HAZ are greater than those in the laser-irradiated zone. Leung et al. (Ref 58) reported that the microhardness of Steel (1050) was higher at the heat-affected zone than at the laser-irradiated zone, and we observe similar results for Al 15.3%Si(wt.%) alloy in our case (Fig. 7a). Results in Fig. 7(b) indicates an exponential curve fitting between crystallite size and microhardness with mathematical formulation as given below,

$$H = H_0 + A. \exp(R_0.x) \qquad (Eq\ 11)$$

With a correlation factor $(R) = 0.998$ and constants, $H_0 = 181.244$, $R_0 = 0.056$, $A = -16.44$. The variable x represents crystallite size, and the dependent variable H indicates the microhardness.

Figure 7(b) indicates that the maximum increase in microhardness (127.6 HV) is seen for HAZ at 300 laser pulses for a minimum value of crystallite size (21.21 nm). At 500 laser pulses, the maximum reduction in microhardness (85.9 HV) is found at the maximum value of crystallite size (31.6 nm). An increase in hardness value can be associated to the modification in dislocation density and variation in grain coarsening that occurred in both HAZ and the laser-irradiated zone. Grain refinement in terms of reduction in grain size causes the enhancement of grain boundary density, which is the reason for the enhancement of the dislocation density. This in return obstructs the dislocation motions which leads to the increase in hardness of the treated samples (Ref 59). Reduced grain size has a significant impact on the mechanical characteristics of crystalline materials. Small grain size enhances a material's strength and improves performance under extreme mechanical requirements. During the middle of the last century around 1950, Hall (1951) and Petch (1953) studied the mechanical properties of materials with grain sizes less than one micrometer, known as ultra-fine grain (UFG), and materials with grain size less than 100 nm, known as nanocrystalline (NC). They individually created the relationship between grain size and yield strength. They discovered that the strength of iron and steel improves when grain size decreases. They summarized their finding as smaller is stronger. Therefore, a reduction in grain size is associated with hardening by the Hall–Petch relationship (Ref 60).

$$H = Ho + KD^{-1/2} \qquad (Eq\ 12)$$

where H is the hardness of the infinite value of the grain, i.e., single crystal, Ho, and K are experimental constants, whereas D is the average crystal grain size. According to Eq 12, microhardness is inversely related to the square root of grain size. This implies that the smaller the grain size, the greater its hardness.

Yet another possible explanation for the increase in surface hardness is the effect of the concentration of silicon in Al alloy. Kalhapure et al. (Ref 61) reported microhardness values for Al-5%Si, Al-7%Si, Al-9%Si, and Al-12%Si as 20 HV, 38 HV, 70 HV, and 85 HV, respectively. This indicates that the hardness of Aluminum improves with the increasing percentage of Silicon. Similar results are observed in our case, a big increment in hardness of Al 15.3%Si(wt.%) is seen (91.47 HV) with a high concentration of silicon in the alloy. Furthermore, with an increase of laser pulses from 400 to 500, the microhardness of the laser-irradiated zone and HAZ is reduced sharply. This is because with a relative increase in laser pulses, re-solidification of melt surface occurs and a more cellular cone like structure (SEM micrographs Fig. 5i and j) was formed in the laser-irradiated zone which results in a drastic increase in grain size (31.6 nm). This pile-up in fine-grained materials and have a smaller number of dislocations, which partially offsets the effect of the grain coarsening and decreases the microhardness of the laser-irradiated zone (Ref 62). These results can be well-correlated with those reported by Maryam et al. (Ref 15), who noted that on increasing laser pulses to a certain extent the values of hardness start to decline.

4. Conclusions

In conclusion, in this work we investigated the influence of laser ablation on the microstructural, morphological, electrical, and mechanical properties of Al 15.3%Si (wt.%). From the

Table 3 Crystallite size, dislocation line density, lattice strain, and electrical resistivity of un-irradiated and laser-irradiated Al-15.3%Si (wt.%) alloy specimens [15]

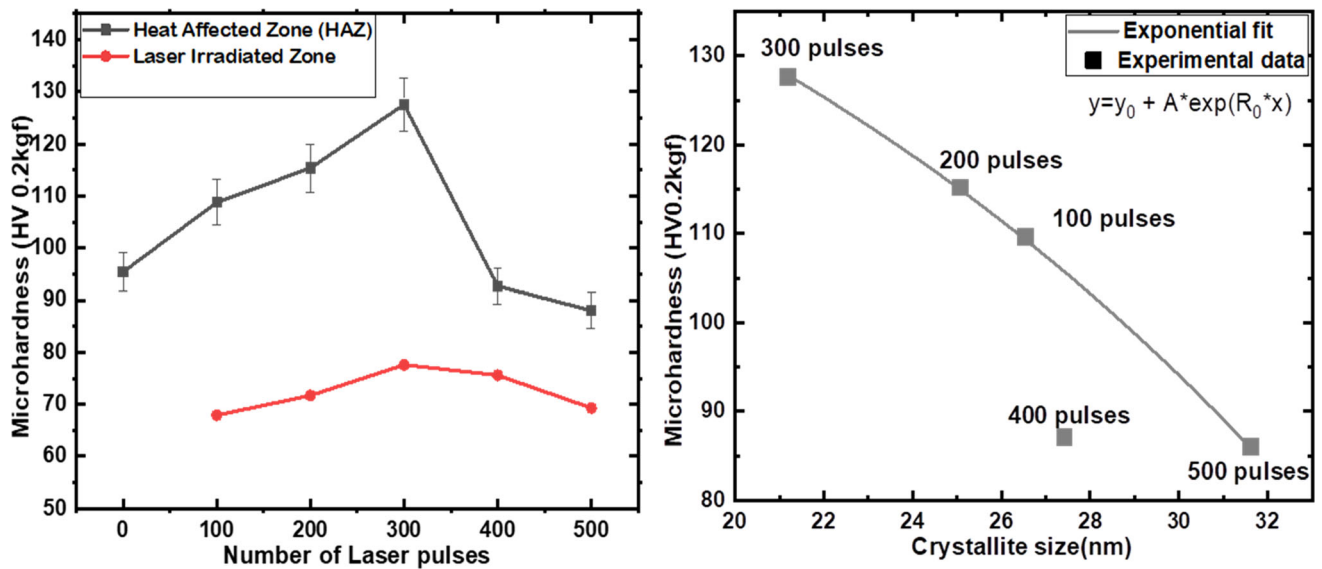| Laser pluses	Crystallite size/grain size, nm	Dislocation line, 10^{14} lines/m^2	Lattice strain	Resistivity, 10^{-7} Ω -m
0	29.4	11.5	0.0123	11.6
100	26.4	14.2	0.0131	15.9
200	25.2	15.7	0.0145	24.8
300	21.2	22.2	0.0161	30.5
400	27.4	13.2	0.0141	14.8
500	31.6	10.0	0.0115	13.6

Fig. 7 (a-b) Microhardness of laser-irradiated zone and Heat-affected zone (HAZ) is displayed as a function of (a) number of laser pulses and (b) crystallite size

Table 4 Microhardness of laser-irradiated zone and heat-affected zone (HAZ) as a function of number of laser pulses

Laser pluses	Avg. hardness (HV) heat-affected zone	Avg. hardness (HV) laser-irradiated zone
0	91.47	60.51
100	108.8	66.13
200	115.4	70.63
300	127.6	80.12
400	87.07	75.51
500	85.91	67.14

XRD results, it is observed that peak intensity, crystalline size, and dislocation density exhibit the anomalous behavior by increasing the laser pulses in the order 100, 200, 300, 400, 500. A reduction in grain size is observed at 300 laser pulses and the maximum value of grain size is found at 500 laser pulses. Surface morphological studies reveal that target alloys are modified by molten material, craters, cones, ripples, and busted bubbles. At 500 laser pulses, unique cellular/columnar microstructures are seen which is the result of the high cooling rate (10 K/s). Electrical resistivity increases from 100 to 300 laser pulses, but at 500 laser pulses, an abrupt decrease in electrical resistivity is observed. The increase in resistivity is greatly influenced by the grain refinement, the smaller the grain size, the higher the frequency of scattering defects for the electrons traveling through the lattice and higher the resistivity of the treated samples. Microhardness measurements revealed that a maximum increase in hardness (127.6 HV) occurred for HAZ at 300 laser pulses. This increase in microhardness can be attributed to decrease in grain size with increasing grain boundaries density that results in hindering the motions of dislocation lines density and causes the enhancement in surface hardness. It is also observed that the hardness value started to decline by increasing the laser pulses from 400 to 500, which can be attributed to the decrease in dislocation line density after the domination of the annealing phenomena by laser irradiation.

References

1. K. Trzcinski, M. Gazda, J. Karczewski, A. Cenian, G.M. Grigorian, and M. Sawczak, "Pulsed Laser Deposition of Bismuth Vanadate Thin Films-The Effect of Oxygen Pressure on the Morphology, Composition, and Photoelectrochemical Performance, *Materials*, 2020, **13**, p 1360
2. A. Piqué, R. Auyeung, H. Kim, A.N. Charipar, and S.A. Mathews, Laser 3D Micro-Manufacturing, *J. Phys. D Appl. Phys.*, 2016, **49**, p 110–118
3. N. Ali, S. Bashir, U.-I. Kalsoom, N. Begumm, and S.W. Ahmad, Surface, Structural and Mechanical Properties of Zirconium Ablated by KrF Excimer Laser Radiation, *Quant. Electron.*, 2016, **46**, p 1015–1022
4. Y.F. Lu, W.D. Song, Z.M. Ren, C.W. An, D.M. Liu, W.J. Wang, B.J. Cho, J.N. Zeng, and C.F. Tan, Advanced Laser Applications in Microelectronics and Data Storage Devices, *J. Laser Appl.*, 2016, **2**, p 12–20
5. G. Anna, I. Ciriolo, R.M. Vázquez, A. Roversi, A. Frezzotti, C. Vozzi, R. Osellame, and S. Stagira, Femtosecond Laser-Micromachining of Glass Micro-Chip for High Order Harmonic Generation in Gases, *Micromachines*, 2020, **5**, p 2–9

6. V.V. Vasilenko, V.I. Polskij, P.S. Dzhumaev, V.N. Petrovskij, and V.L. Yakushin, Surface Hardening Low Alloy Structural Steel by Laser Welding, in 15th International School-Conference New Materials-Materials of Innovative Energy: Development, Characterization Methods and Application, *KnE Mater. Sci.*, 2017, **6**, p 440–450

7. C.S. Petrovi, S.D. Peru, P. Pelicon, C.J. Kova, and C.M. Mitri, Laser-Induced Surface Alloying in Nanosized Ni/Ti Multilayer Structures, *Appl. Surf. Sci.*, 2013, **264**, p 273–279

8. E.A. Starke Jr. and J.T. Staley, Application of Modern Aluminum Alloy to Aircrafts, *Prog. Aerosp. Sci.*, 1996, **32**, p 131–172

9. Y. Yang and J.D. Hu, Effects of Laser Power Density on the Microstructure and Microhardness of Ni-Al Alloyed Layer by Pulsed Laser Irradiation, *Opt. Laser Technol.*, 2011, **43**, p 138–142

10. J. Susnik, R. Sturm, and J. Grum, Influence of Laser Surface Remelting on Al-Si Alloy Properties, *J. Mechan. Eng.*, 2012, **58**, p 614–620

11. A. Biswas, B.L. Mordike, I. Manna, J. Dutta Majumda, A.F.M. Arif, C. Karats, and K. Raza, Studies on Laser Surface Melting of Al-11% Si Alloy, *Lasers Eng.*, 2009, **8**, p 95–105

12. A. Nassar, M.A. Taha, and F.A. Saadallah, Surface Hardening of Hypereutectic Al- Si Alloy Treated by Nd: YAG Laser, *Middle East J. Appl. Sci.*, 2015, **5**, p 31–35

13. A.T. Zayed, *Laser Surface Treatments of Steel and Aluminum Alloys*, Thesis, Baghdad University, Baghdad, M.Sc, 2003

14. S.A. Mohammed, Study the Effect of Laser Surface Treatment On Aluminum Alloys. M. Sc. Thesis, University of Technology, Baghdad, (2004)

15. S. Maryam and F. Bashir, Effect of Laser Irradiation on Surface Hardness and Structural Parameters of 7178 Aluminium Alloy, *Mater. Res. Exp.*, 2018, **5**, p 1–9

16. M.K. Abbas and A.K. Mahmoud, Laser Surface Treatment of Al-12%Si Alloy, *Mater. Today Proc.*, 2017, **4**, p 9992–9996

17. K. Nayat and S. Oskayama, Penetration and Energy-Loss Theory of Electrons in Solid Targets, *J. Phys. D Appl. Phys.*, 1972, **5**, p 43–57

18. Z. Wang, H. Wang, X. Li, D. Wang, Q. Zhang, G. Chen, and Z. Ren, Aluminum and Silicon Based Phase Change Materials for High Capacity Thermal Energy Storage, *Appl. Thermal Eng.*, 2015, **89**, p 204–208

19. B. Dang, Z. Jian, J. Xu, and S. Li, Density and Solidification Shrinkage of Hypereutectic Al–Si Alloys, *Int. J. Mater. Res.*, 2017, **10**, p 815–819

20. B.M. Angadi and C.R. Hiremath, Studies on the Thermal Properties of Hypereutectic Al–Si Alloys by Using Transient Method, *J. Mechan. Eng. Res. Technol.*, 2014, **2**, p 536–544

21. U.-I. Kalsoom, N. Ali, S. Bashir, A.M. Alsheri, and N. Begaum, Study of Micro/Nano Structuring and Mechanical Properties of KrF Excimer Laser Irradiated Al for Aerospace Industry and Surface Engineering Applications, *Materials*, 2021, **14**, p 1–22

22. F.B. Meng, H.J. Huang, X.G. Yuan, Z.W. Cui, and X.L. Hu, Effect of Si Addition on Microstructure and Mechanical Properties of Al-Mg-Si-Zn Alloy, *Res. Develop.*, 2020, **17**, p 15–20

23. H. Latif, M.S. Rafique, M. Shahid, K.-U. Rahaman, M. Rawat, R.S. Sattar, A.N. Shahzad, and P. Lee, Impact of Laser Produced X-rays on the Surface of Gold, *Appl. Surface Sci.*, 2008, **254**, p 7505–7511

24. J.W. Yeh, S.Y. Chang, Y.D. Hong, S.K. Chen, and S.J. Lin, Anomalous Decrease in X-ray Diffraction Intensities of Cu–Ni–Al–Co–Cr–Fe–Si Alloy Systems with Multi-Principal Elements, *Mater. Chem. Phys.*, 2007, **103**, p 41–45

25. J.M. Myoung, W.H. Yoon, D.H. Lee, I. Yun, S.H. Bae, and S.Y. Lee, Effects of Thickness Variation on Properties of ZnO Thin Films Grown by Pulsed Laser Deposition, *Japan. J. Appl. Phys.*, 2002, **41**, p 28–31

26. B.D. Cullity and S.R. Stock, Elements of X-ray Diffraction 3rd ed Prentice Hall, Englewood Cliffs, NJ, p. 388 (2001)

27. S. Venkatachalam, R. Kumar, D. Mangalaraj, S.K. Narayandass, K. Kim, and J. Yi, Optoelectronic Properties of Zn0.52Se 0.48/Si Schottky Diodes, *Solid-State Electron.*, 2004, **48**, p 2219–2223

28. A.R. Stokes and A.J.C. Wilson, The Diffraction of X Rays by Distorted Crystal Aggregates-I, *Proc. Phys. Soc.*, 1943, **56**, p 174–181

29. N. Ali, S. Bashir, M. Umm-i-Kalsoom, and K.M. Akram, Effect of Dry and Wet Ambient Environment on the Pulsed Laser Ablation of Titanium, *Appl. Surface Sci.*, 2013, **270**, p 49–57

30. F. Lasagni and H.P. Degischer, Enhanced Young's Modulus of AlSi Alloys and Reinforced Matrices by Co-continuous Structures, *J. Compos. Mater.*, 2010, **44**, p 740–755

31. J. Gubicza, Correlation between Processing Conditions, Lattice Defect Structure and Mechanical Performance of Ultrafine-Grained Materials, *Proc. Int. Sympos. Phys. Mater.*, 2015, **128**, p 479–486

32. F. Zhou, X.Z. Liao, Y.T. Zhu, S. Dallek, and E.J. Lavernia, Microstructural evolution during recovery and recrystallization of a nanocrystalline Al-Mg alloy prepared by cryogenic ball milling, *Acta Mater.*, 2003, **51**, p 2777–2791

33. F. Suna, S. Bhattacharyaa, G.P. Dindac, A. Dasguptac, and J. Mazumdera, "Influence of Processing Parameters on Lattice Parameters in Laser Deposited Tool Alloy Steel, *Mater. Sci. Eng.*, 2011, **15**, p 5141–5145

34. A. Latif, M. Khaleeq-Ur-Rahman, K. Bhatti, M. Rafique, and Z. Rizvi, IR and UV Irradiations on Ion Bombarded Polycrystalline Silver, *Phys. B Condens. Matter.*, 2010, **405**, p 4250–4255

35. V.N. Gurarie, P.H. Otsuka, D.N. Jamieson, and S. Prawe, Crack-Arresting Compression Layers Produced by Ion Implantation, *Nuclear Inst. Methods Phys. Res. Sect. B Beam Int. Mater. Atoms*, 2006, **242**, p 421–423

36. U.-I. Kalsoom, R. Ahmad, N. Ali, I.A. Khan, S. Saleem, U. Ikhlaq, and N. Khan, Effect of Power and Nitrogen Content on the Deposition of CrN Films by Using Pulsed DC Magnetron Sputtering Plasma, *Plasma Sci. Technol.*, 2013, **15**, p 666–672

37. S. Juodkazis, K. Nishimura, S. Tanaka, H. Misawa, E.G. Gamaly, B.L. Davies, L. Hallo, P. Nicolai, and V.T. Tikhonchuk, Laser-Induced Microexplosion Confined in the Bulk of a Sapphire Crystal Evidence of Multimegabar Pressures, *Phys. Rev.*, 2006, **96**, p 166101

38. S. Kradolfer, K. Heutschi, J. Koch, and D. Günther, Tracking Mass Removal of Portable Laser Ablation Sampling by its Acoustic Response", *Spectroch. Acta Part B Atom. Spectros.*, 2021, **179**, p 106118

39. M. Jelani, S. Bashir, M. Khaleeq-ur-Rehman, R. Ahmad, Y.D. Faizan-ul-Haq, M. Akram, N. Afzal, M.U. Chaudhry, K. Mahmood, and A. Hayat, Effect of Laser Fuence on Surface, Structural and Mechanical Properties of Zr After Irradiation in the Ambient Environment of Oxygen, *Europ. Phys. J. D*, 2013, **67**, p 159

40. D. Yousaf, S. Bashir, M. Akram, U.-I. Kalsooma, and N. Ali, Laser Irradiation Effects on the Surface, Structural and Mechanical Properties ofAl–Cu Alloy 2024, *Radiat. Effects Defects Solids.*, 2013, **169**, p 144–156

41. W. Li, S. Li, J. Liu, A. Zhang, Y. Zhou, C. Wei, C. Yan, and Y. Shi, Effect of Heat Treatment on AlSi10Mg Alloy Fabricated by Selective Laser Melting: Microstructure Evolution, Mechanical Properties and Fracture Mechanism, *Mater. Sci. Eng. A*, 2016, **663**, p 116–125

42. E. Lee and B. Mishra, Effect of Solidification Cooling Rate on Mechanical Properties and Microstructure of Al-Si-Mn-Mg Alloy, *Mater. Trans.*, 2017, **58**, p 1624–1627

43. M.S. Rafique, M.K. Rahman, T. Firdos, K. Aslam, M.S. Anwar, M. Imran, and H. Latif, XRD and SEM Analysis of a Laser-Irradiated Cadmium, *Laser Phys.*, 2007, **17**, p 1–7

44. X. Wang and X. Xu, "Thermoplastic Waves Induced by Pulsed Laser Heating, *Appl. Phys. A*, 2001, **73**(1), p 107–114

45. L.L. Bin, L.T. Cheng, L. Yong, and L. Qiang, Variation of Morphology and Color of VO$_2$ thin Films Induced by Excimer Laser", *Nuclear Instrum, Methods Phys. Res. Sect. B*, 2002, **191**, p 102–105

46. K. Zhang and G.N. Chen, "Grain Structure of Laser Remelted 7075 Aluminium Alloy in Presence of Al2O3 Particles, *Mater. Sci. Technol.*, 2001, **17**, p 668–670

47. H. Zhang, Z. Zhang, and T.M. Yue, The Pseudo-Eutectic Microstructure and Enhanced Properties in Laser-Cladded Hypereutectic Ti–20%Si, *Coat. Metals.*, 2017, **7**, p 33

48. G.P. Dinda, A.K. Dasgupta, and J. Mazumder, Evolution of Microstructure in Laser Deposited Al-11.28%Si Alloy, *Surface Coat. Technol.*, 2012, **206**, p 2152–2160

49. M.Z. Butt, M. Dilawar Ali, S. Usman, and T. Naseem, Surface Roughness and Electrical Resistivity of High-Purity Zinc Irradiated with Nanosecond Visible Laser Pulses, *Appl. Surface Sci.*, 2014, **305**, p 466–473

50. A. Latif, K.A. Bhatti, M. Khaleeq-Ur-Rahman, and M.S. Rafique, Effect of UV Irradiation on the Structural, Optical and Electrical Properties of Platinum, *Radiat. Effects Defects Solids*, 2012, **167**, p 929–936

51. S. Bashir, M.S. Rafique, M. Khaleeq-Ur Rahman Faizan ul Haq, and B.R. Alvina, CO$_2$ and Nd:YAG Laser Radiation Induced Damage in Aluminum. 15, 181–192 (2006)

52. H. Bishara, S. Lee, T. Brink, M. Ghidelli, and G. Dehm, Understanding Grain Boundary Electrical Resistivity in Cu: the Effect of Boundary Structure, *ACS Nano*, 2021, **15**, p 16607–16615

53. M. Vopasroiu, M.J. Thwaites, G.V. Fernandez, S. Lepadtu, and K.O. Grady, Grain Size Effects in Metallic Thin Films Prepared Using A New Sputtering Technology, *J. Optoelectron. Adv. Mater.*, 2005, **7**, p 2713–2720

54. O. Ivanov, O. Maradudina, and R. Lyubushkin, Grain size Effect on Electrical Resistivity Electrical Resistivity of Bulk Nano-Grained Bi_2Te_3 Material, *Mater. Characteriz.*, 2015, **99**, p 175–179

55. M.Z. Butt, D. Ali, F. Bashir, and M. Ishtiaq, Effects of IR Laser Shots on the Surface Hardness and Electrical Resistivity of High-Purity Iron, *J. Mater. Eng. Perform.*, 2014, **23**, p 772–777

56. H. Kaya, U. Boyuk, E. Cadırli, and N. Marasli, Measurements of the Microhardness, Electrical and Thermal Properties of the Al-Ni Eutectic Alloy, *Mater. Des.*, 2012, **34**, p 707–712

57. H. Kaya, U. Boyuk, E. Cadırli, and N. Marasli, Influence of Growth Rate on Microstructure, Microhardness, and Electrical Resistivity of Directionally Solidified Al-7 wt.% Ni Hypo-Eutectic Alloy, *Metals Mater. Interact.*, 2013, **19**, p 39–44

58. K.H. Michael and J.K. Yu Leung, Theoretical and Experimental Studies on Laser Transformation Hardening of Steel by Customized Beam, *Int. J. Heat Mass Transfer*, 2007, **50**, p 4600–4606

59. S.N. Naik and S.M. Walley, The Hall Patch and Inverse Hall Patch Relations and the Hardness of Non-Crystalline Metals, *J. Mater. Sci.*, 2020, **55**, p 2661–2681

60. R.R. Baracaldo, J.M. Cabrera Marrero, and J.A.B. Páramo, Studying the Hall-Petch Effect Regarding Sub-Micrometer Steel (0.6% C), *Ingen. Investigat.*, 2011, **31**, p 112–120

61. M.G. Kalhapure and P.M. Dighe, Impact of Silicon Content on Mechanical Properties of Aluminum Alloys, *Int. J. Sci. Res. (IJSR)*, 2013, **4**, p 38–40

62. M.Z. Butt, F. Bashir and S. Arooj, Effect of UV Laser Irradiation on the Hardness and Structural Parameters of Ag_xPd_{1-x} ($0.4 \leq x \leq 0.6$) Alloys, *Appl. Surf. Sci.*, 2012, **259**, p 740–746